Journal of Power Sources 241 (2013) 379–387

Contents lists available at SciVerse ScienceDirect

Journal of Power Sources

journal homepage: www.elsevier.com/locate/jpowsour

Deterministic contact mechanics model applied to electrode interfaces in polymer electrolyte fuel cells and interfacial water accumulation

I.V. Zenyuk [a], E.C. Kumbur [b], S. Litster [a,*]

[a] Department of Mechanical Engineering, Carnegie Mellon University, Pittsburgh, PA 15213, USA
[b] Department of Mechanical Engineering and Mechanics, Drexel University, Philadelphia, PA 19104, USA

HIGHLIGHTS

- Deterministic contact mechanics model applied to catalyst layer|MPL interface.
- Direct imaging of sample surface topology for true morphology.
- The cracked CL|MPL interface can store more water than the uncracked.
- Cracks cover little contact area and cause minimal interfacial resistance.
- van Genuchten water retention correlation shows a good agreement.

ARTICLE INFO

Article history:
Received 12 November 2012
Received in revised form
4 February 2013
Accepted 25 March 2013
Available online 20 April 2013

Keywords:
Contact mechanics model
Water retention curve
van Genuchten correlation
Catalyst layer micro-porous layer interface
Polymer electrolyte fuel cell
Capillary pressure

ABSTRACT

An elastic deterministic contact mechanics model is applied to the compressed micro-porous (MPL) and catalyst layer (CL) interfaces in polymer electrolyte fuel cells (PEFCs) to elucidate the interfacial morphology. The model employs measured two-dimensional surface profiles and computes local surface deformation and interfacial gap, average contact resistance, and percent contact area as a function of compression pressure. Here, we apply the model to one interface having a MPL with cracks and one with a crack-free MPL. The void size distributions and water retention curves for the two sets of CL|MPL interfaces under compression are also computed. The CL|MPL interfaces with cracks are observed to have higher roughness, resulting in twice the interfacial average gap compared to the non-cracked interface at a given level of compression. The results indicate that the interfacial contact resistance is roughly the same for cracked or non-cracked interfaces due to cracks occupying low percentage of overall area. However, the cracked CL|MPL interface yields higher liquid saturation levels at all capillary pressures, resulting in an order of magnitude higher water storage capacity compared to the smooth interface. The van Genuchten water retention curve correlation for log-normal void size distributions is found to fit non-cracked CL|MPL interfaces well.

1. Introduction

Polymer electrolyte fuel cells (PEFC) are promising power source devices for a wide variety of portable, automotive, and stationary applications. To achieve cost-effective mass-production of these low-emission devices, certain technological challenges have to be resolved [1]. Ohmic and mass transport losses at the interface of catalyst layer (CL) and micro-porous layer (MPL) have not been studied widely but recent experimental studies show that this interface plays a critical role in electrode structure and performance [2–6]. The imperfect interfacial contact of the CL and MPL can create high resistance pathway for electron transport, whereas the resulting interfacial voids can lead to liquid water pooling. Water accumulation at the CL|MPL interface is not desirable due to a hindrance of reactant gas transport to the electrode's active reaction sites and the resulting loss of fuel cell performance. Gaining a further insight into Ohmic and mass transport limitations of the interface requires better understanding of the morphologies of the CL and MPL as well as the CL|MPL interface topologies under varying compression.

Due to the minute length scales and experimental limitations, mathematical models are valuable tools often used in evaluating multiphase transport phenomena in PEFC materials. Modeling

* Corresponding author. Scaife Hall 323, 5000 Forbes Avenue, Pittsburgh, PA 15213, USA. Tel.: +1 412 268 3050.
E-mail address: litster@andrew.cmu.edu (S. Litster).

0378-7753/$ – see front matter © 2013 Elsevier B.V. All rights reserved.
http://dx.doi.org/10.1016/j.jpowsour.2013.03.165

water transport through porous carbon substrates, such as diffusion media (DM) and MPL typically requires water retention curves. These are the correlations that relate capillary pressure to saturation; the most common correlations are reviewed by Gostick et al. [7] and Litster and Djilali [8]. These water retention curves include the Brooks-Corey [9], van Genuchten [10] and Udell [11] correlations, where the van Genuchten correlation is based on the reasonable assumption of a log-normal void size distribution. There is also a family of empirical correlations for water retention curves, such as Udell [11] functions, which are derived based on empirical data obtained by Leverett. There have been several experimental and computational studies reporting water retention curves for the DM and MPL [7,12,13] but none for the CL|MPL interface. Although, some researchers have previously included finite computational region for the MPL|DM interface [14–16], the interface between the MPL and CL is treated as an infinitely thin layer in most modeling studies.

There have been several experimental [17,18] and one analytical work [19] done to investigate the CL|MPL contact resistance. Kleemann et al. [17] used a 4-point device applying current across the CL|MPL interface and measured potential drop. They back-calculate the contact resistance using an electrical finite element simulation with the measured electric potential difference across the device as an input. They showed decreasing trend of contact resistance with increasing compression pressure, however they were not able to separate the MPL resistance from the contact resistance. Swamy et al. [19] developed an analytical model that computes contact resistance and estimates the maximum capacity for water accumulation at the interface at different compressions. They used statistical approach where key interfacial model parameters, such as summit density, standard deviation, and radius of the summit, were extracted from their optical profilometry data. To the best of our knowledge, there is no prior work on using actual CL and MPL morphology to computationally reconstruct the three-dimensional interfacial morphology under varying compression.

There have been numerous theoretical studies focused on understanding the interfacial roughness in the field of tribology [20–29]. Historically, two major frameworks (i.e., statistical and deterministic) have been developed to model the elastic–plastic interfacial contact. The statistical framework was pioneered by Greenwood and Williamson [30] (GW) to elucidate the relationship between the applied load and average gap for rough materials. Typically, the statistical approach approximates the surface summits using average parameters for their density, radius and curvature. The advantages of the statistical approach include its computational efficiency and the ease of calculating area-averaged interfacial parameters. However, the statistical models do not provide information about local gap, surface deformation and asperity contact pressure.

In contrast to the statistical approach, deterministic models use actual measured or generated surface profile data and predict local and area-average interface properties. Johnson et al. [20] developed an asymptotic three-dimensional solution to an interface featuring a sinusoidal surface pressed against a flat surface. In the following decades, the contact mechanics problems of real rough surfaces were solved using a matrix of influence coefficients, which relates contact pressure and deformation [24,25,27]. However, for three-dimensional surfaces the matrix's computational and storage expense were high- pressing for an alternative solution methodology. Solution procedures based on minimization of total complementary energy [28] utilizing a fast Fourier transform (FFT) [25,28,29] and convolution theorem has proved to be economic in data storage and efficient in computation.

Here we present a numerical elastic deterministic contact mechanics model that predicts average properties as well as local deformation, pressure and separation distance at the three-dimensional CL|MPL interface under different compressions. We image two different sets of CLs and MPLs using an optical microscope, characterize surfaces roughness, and then input three-dimensional CL and MPL surface profiles into the contact mechanics model. Water retention curves are generated based on the model predictions for the void size distributions of the two sets of interfaces.

2. Contact mechanics model

We use deterministic contact mechanics modeling approach proposed by Hu et al. [28] to resolve the local deformation of contacting asperities under applied pressure. The following assumptions were used in the present contact mechanics model:

- the surfaces deform elastically: the local strains are small and plastic deformation is neglected;
- the surfaces of MPL and CL are large enough to be treated as half-spaces;
- the magnitude of normal contact pressure is assumed to be much higher than the tangential forces because the MEA is very thin and the area of compression is large;
- zero intrusion is assumed between the CL and MPL surfaces.

Fig. 1 is a two-dimensional schematic of the MPL and CL surfaces prior and after deformation. In the figure, $\bar{\delta}$ is the separation distance between the two undeformed surfaces when a load is applied, whereas δ is the gap between the deformed surfaces. Based on a half-space Boussinesq solution, the composite vertical surface displacement, $u(x,y)$, at a point (x,y) of two surfaces under the normal pressure field $p(x',y')$ is given by:

$$u(x,y) = \frac{2}{\pi E_{eq}} \iint_{\Omega} p(x',y')K(x'-x,y'-y)\mathrm{d}x'\mathrm{d}y' \tag{1}$$

where $K(x,y)$ represents surface deformation distribution under an applied contact unit load acting at the origin. For the elastic half-space surfaces, the kernel $K(x,y)$ is given by Boussinesq solution:

$$K(x',y') = \frac{1}{\sqrt{x'^2+y'^2}} \tag{2}$$

and where E_{eq} is the equivalent Young's modulus of the two surfaces defined as:

$$E_{eq} = \left[\frac{1}{2}\left(\frac{1-\nu_{CL}^2}{E_{CL}} + \frac{1-\nu_{MPL}^2}{E_{MPL}}\right)\right]^{-1} \tag{3}$$

where ν is Poisson's ratio.

The force–displacement relation of Eq. (1) can be solved with matrix multiplication: $u = C \cdot p$, where C is the matrix of influence coefficients. This matrix has to be determined in advance by

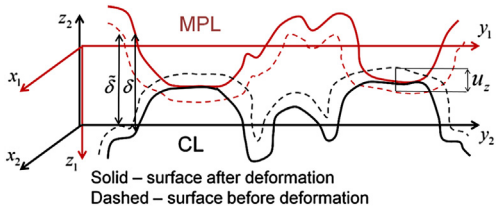

Fig. 1. Schematic of asperities and model parameters at the CL|MPL interface.

interpolation function to the integral of Eq. (1) or alternatively by Green's function. The difficulty in determining the matrix of influence coefficients is the singularity in the solution at a point where the load is applied. By representing Eq. (1) in discrete form and assuming that within each discrete element the pressure distribution is uniform, Love [31] derived an expression that avoids the solution singularity and presents an explicit form for the matrix of influence coefficients, which we utilize in our model (see Supplemental material).

Solving Eq. (1) through direct matrix multiplication is computationally expensive due to large number of operations in computing C and its demanding storage requirements. In our work we use a FFT convolution theorem to solve Eq. (1) that is more efficient, having reduced computational operations and lower storage requirements. The difficulty in using the FFT-approach lies in the fact that the convolution theorem requires two conditions to be met: periodicity and infinite domain [32]. Utilizing techniques of zero-padding and wrap-around order we were able to meet these criteria and eliminate aliasing error [32,33]. We also verified the FFT-approach by simulating the analytical solution of Johnson [20], who studied the contact problem of a flat plane and isotropic wavy surface (see Supplemental material). The only error that the FFT-approach produced was a 1–2% discretization error.

The solution to the force–displacement relation described by Eq. (1) requires the knowledge of pressure or deformation distributions. Commonly, one uses linear complementary problem (LCP) [34] with constraints to describe the elastic-deformation problem. The standard matrix form of which is:

$$\begin{cases} \delta = \bar{\delta} + C \cdot p \\ \delta_i \geq 0, \;\; p_i \geq 0, \;\; \delta_i \cdot p_i = 0, \quad i = 1, 2, \ldots, N \end{cases} \tag{4}$$

The first constraint of non-negative pressure and surfaces separation distance is derived from the assumption of no surface overlap. The second constraint states that the surface gap has to be zero if the contact pressure is positive and the surface gap has to be positive if the contact pressure at the point is zero. There are numerous methods and iteration schemes that provide LCP solutions with the FFT-approach for computing influence matrix coefficients. Here, we use a conjugate gradient method (CGM) to solve Eq. (4). The details of this procedure are given by Hu et al. [28] Fig. 2 shows a flowchart of the solution procedure. The model's input is the discrete set of height data from the optical microscope and the initial surfaces approach (or alternatively clamping force). The output of the model is the local non-dimensional contact pressure, deformation, and the half-space separation distance between the MPL and CL. To avoid the uncertainty of Young's modulus and Poisson's ratio for these PEFC materials, we keep the contact pressure in a non-dimensional form, normalizing it by equivalent Young's modulus described with Eq. (3):

$$p/p^* = p/E_{\text{eq}} \tag{5}$$

3. Experimental

We characterize the surfaces of the MPL and CL using an optical microscopy technique that yields three-dimensional reconstructions of the surface profiles. The technique uses an XYZ automated stage (Prior ProScan III, Prior Scientific, Rockland, MA) on an upright microscope (Nikon LV Microscope LV 100, Nikon Instruments Inc., Melville, NY) with a 50× objective (LU Plan BD ELWD, NA = 0.55, Nikon Instruments, Inc.) to scan over large areas and perform local z-stacking. By determining the in-focus areas at each z-height with extended depth of field algorithm, a 3D surface

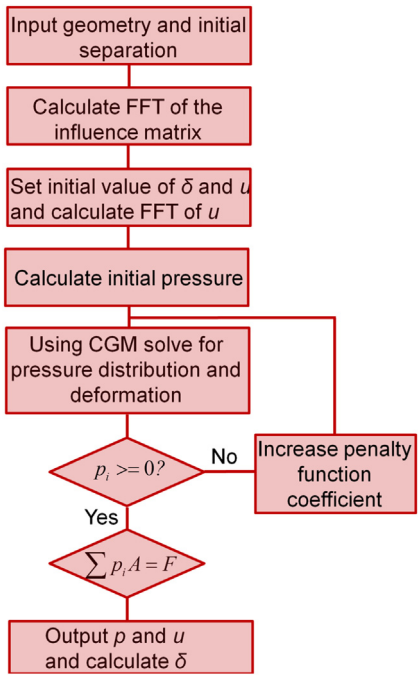

Fig. 2. Flowchart of numerical procedure for the deterministic contact mechanics model.

can be generated. More precisely, we use the 'Scan Large Image With Z' function in a commercial software package (NIS-Elements AR 3.2, Nikon Instruments Inc.) to automate the process where the dimensions in X–Y–Z are specified. The microscope automation program then images the entire sample area-by-area, as dictated by the objective's smaller field of view, performing z-stack on each individual area, and then stitches the areas together using specified overlap percentage. For our experiment, we set the overlap to be equal to 0. The pixel calibration is 0.1036 μm/px, whereas the z-step is set to 1.68 μm. The size of one image is 172 × 139 μm and the large image is stitched with up to 120 small images (10 by 12 images in x and y).

There are several advantages and disadvantages to surface characterizations using optical microscope with z-stacking as listed below.

Advantages:

- The horizontal resolution is good (<1 μm) and comparable to an optical profilometer [35].
- Large area images can be stitched on an automated stage, although areas greater than 1 cm^2 will be time-consuming and computationally expensive at the current level of resolution.
- Samples are not modified or damaged by imaging (no sputtering or focused ion beam milling) and can subsequently be used in fuel cell experiments or in further characterizations.

Disadvantages:

- The vertical resolution is on order of 1 μm due to the depth of field limitations.
- The microscope does not image details below the surface or under overhangs.

The surfaces of two MPLs on carbon diffusion media and two commercial CLs were investigated. The two MPL samples studied are those of a SGL 10BC Sigracet GDL (SGL Group, Wiesbaden,

Germany), abbreviated as SGL, and a MRC U105 carbon paper with an MPL, abbreviated as MRC. The CLs studied are from an Ion Power MEA (Ion Power, Inc., New Castle, DE), abbreviated as IP, and from a Gore Primea MEA (W.L. Gore & Associates, Inc., Newark, DE), abbreviated as Gore. We chose the size of the imaging area to sufficiently represent average surface topology of the sample. Due to anisotropy and cracked nature of the SGL MPL sample, the large scanned image consisted of 120 small images amounting to total area of 1720 × 1670 μm. The CL samples were more isotropic with less large scale structure. Thus, only 30 (5 by 6) CL images were stitched together to reduce imaging time.

Once the imaging was complete, we used commercial microscope software (NIS-Elements AR 3.2, Nikon Instruments Inc.) to create the focused image with spatially-resolved height data. We extracted the discrete height matrix for a given focused image and exported it to Matlab. One can control the resolution of the x–y mesh when exporting the height data and for our samples the distance between the data values in x and y directions was set equal to 1.16 μm. We mounted the samples without applying compression or in-plane tension, which resulted in a sample that was not perfectly flat. To correct for this large length scale effect, we subtract a 2D linear plane fit through the discrete height data of the samples using the 'detrend' function in MATLAB.

4. Results

4.1. Surfaces roughness analysis

Fig. 3a–d shows large focused images of SGL, IP, MRC and Gore, respectively. One can observe the change in image intensity near the edges of the smaller images that are stitched together. The morphology is extracted from the focused height at each location rather than intensity and thus the intensity changes near the borders have no significant impact on the overall height profile. One observes cracks and protruded fibers on the surface of the SGL sample shown in Fig. 3a. The cracks seem to be randomly oriented with widths as large as 50 μm and lengths as long as 1.4 mm. The protruding fibers from the GDL are visible on the several locations outside the cracks. They are also seen inside the cracks possibly indicating that the depth of the crack is equivalent to the MPL thickness. One observes hills and valleys on the surface of the MRC shown by Fig. 3c, however no deep cracks or protruding fibers. The two CL surfaces studied are shown in Fig. 3b and d. They are observed to be relatively flat. The brighter spots on the images most likely correspond to large platinum aggregates.

To gain a more quantitative understanding of surface morphology, we analyzed the large image data with using a variety of statistical techniques. Fig. 3e–h shows three-dimensional reconstructions of the samples. The plane representing the mean height value is centered at $z = 0$ axis. The cracks and peaks of the surfaces are well resolved. The roughness amplitude statistics were computed from the samples' height data. Table 1 lists the five different statistics and their formulas used to characterize the MPL and CL surface samples [36]. These parameters are referenced with respect to the median of the data and are computed over the entire area. All the roughness amplitude parameters indicate that the MPLs are rougher than CLs. In particular, the SGL surface has cracks as deep as 133 μm and fibers protruding up to 59 μm from the diffusion media. Our amplitude parameters for the SGL and CLs are within a range of those calculated by Hizir et al. [35] who characterized similar surfaces using optical profilometry.

To further characterize surface morphology of the MPL and CL samples, we computed average radial power spectra density (psd), the mathematical definition of which is described in detail elsewhere [37]. First, the 2D FFT of the height profile was computed, shifted to have zero-frequency component at the center of the spectrum and then normalized by the x–y area. We retrieved the Fourier coefficients and computed the power of the positive half of the frequency range. Then, starting from the center of the frequency domain and going outward with an increment of $\Delta r = 1.2$ μm we computed the mean of the psd for a given radius. Finally, we plot the mean psd as a function of vector frequencies, $k = 1/r$.

Fig. 4a shows log–log plots of the psd of height for the MPLs. The psd plot exhibits linear profiles on several intervals. It is reasonable to assume that a frequency of around 10^{-1} μm^{-1} that corresponds to $r = 10$ μm separates the regions of large and small-scale surface morphological features. Due to limited resolution the small-scale features might not be resolved, however the large-scale morphologies can be characterized by linear fits through the psd plots in a frequency range lower than 10^{-1} μm^{-1}. The values of the r that

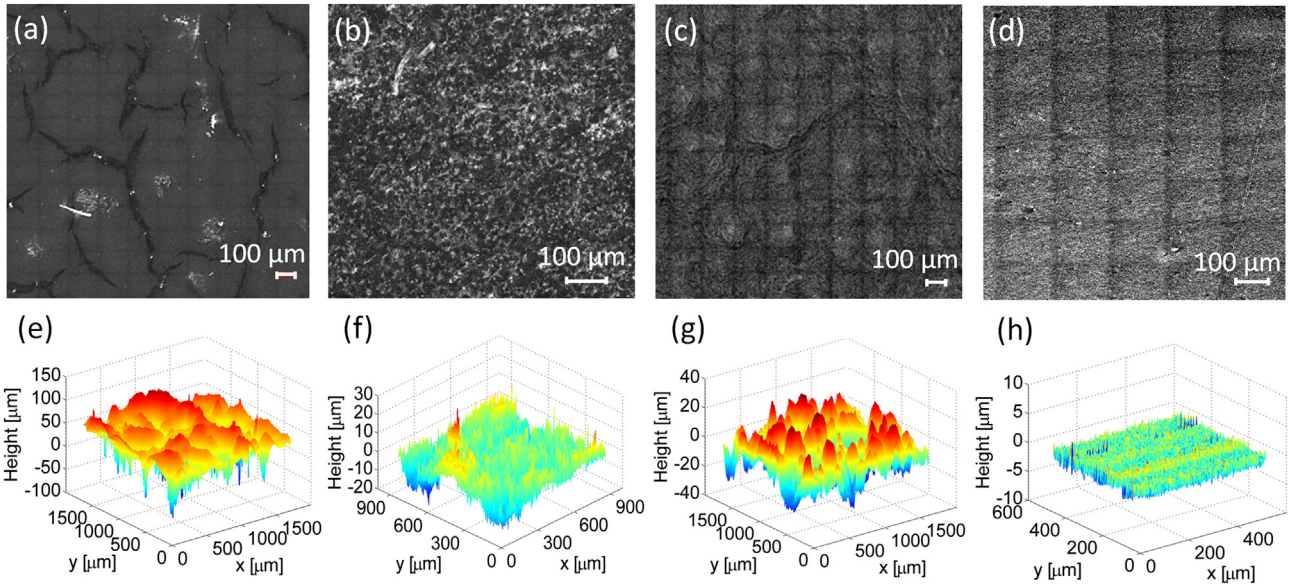

Fig. 3. Stitched optical micrographs of the SGL 10BC MPL (a), Ion Power CL (b), MRC MPL (c) and Gore CL (d) as well as the corresponding 3D surface heights (e), (f), (g) and (h).

Table 1
Roughness results for the CL and MPL samples.

Roughness	Average	Root mean square	Max. Profile peak height	Max profile valley depth	Max. Height of the surface
Formula	$R_a = \frac{1}{MN}\sum_{j=1}^{M}\sum_{i=1}^{N}\lvert Z_{ij}\rvert$ [μm]	$R_q = \sqrt{\frac{1}{MN}\sum_{j=1}^{M}\sum_{i=1}^{N}\lvert Z_{ij}^2\rvert}$ [μm]	$R_p = Z_{\max,\text{peak}}$ [μm]	$R_v = Z_{\max,\text{depth}}$ [μm]	$R_t = Z_{\max,\text{peak}} + \lvert Z_{\max,\text{depth}}\rvert$ [μm]
Gore	0.0633	1.03	2.92	2.07	5.01
IP	0.125	3.56	29.1	20.8	50.04
MRC	0.618	9.43	43.1	29.5	72.7
SGL	3.52	23.89	59.32	133.3	192.6

correspond to frequencies of around 10^{-3} μm^{-1} are on the same order of magnitude as the samples' dimensions. Larger sample data is required to resolve these long-scale frequencies properly. With the current data set that does not have enough data points in the low-frequency regime the psd will have a flat profile there. We use the power law to create the linear fits into these psd plots, where the psd behaves like $k^{-\beta}$ – frequency to a power β. Such scaling arises in many natural systems and materials [38–40]. For reference, white noise (flat psd) has a β value of 0 and Brownian motion has a β value of 2. Several linear regions indicate that there might be different frequency regions or larger and smaller-scale physical phenomenon present. For the two MPL samples, the low-frequency ($k < 0.1$, or length scales greater than 10 μm) profile has β value of 3.0 for the SGL sample and 3.1 for the MRC.

Fig. 4b shows the psd profiles for the two CL samples. Similar to the MPL data analysis, we use linear fits to characterize the data at low frequencies. For the IP sample, β was found to be 2.3, whereas for the Gore sample it was 1.9 – these are smaller values than the exponents found for the MPLs. The β value could potentially be a valuable single value figure of merit in evaluating interface morphologies, where greater values indicate a greater relative roughness at larger scales. In other words, in the case of a high β value, if the large and small scale features are normalized to the same scale by their amplitude, the large scale feature will appear rougher and the small scale structure smoother. If the β value is ~1 there is scale-invariance and all scales present similar roughness.

At low frequencies (longer length scales) the magnitude of the psd is higher for the MPLs compared to the CLs, which is consistent with the MPLs' larger features. The low-frequency psd magnitude of the Gore sample is about three-four magnitudes lower than those of the MPL samples. It can be attributed to the negligible large scale surface roughness, such as hills or cracks, in the Gore sample. Additionally, the SGL and IP materials have nearly identical psd profiles for $k > 0.02$ μm^{-1} ($l < 50$ μm). This range corresponds to small scale roughness due to the agglomerated carbon particles, which is smaller than the length scale associated with hills and valleys or cracks. It is also notable that the Gore and MRC psd values are also significantly lower at higher frequencies (short length scales) compared to the IP and SGL. These differences at the small scale are likely the result of differences in the constituent materials and proprietary processing techniques.

4.2. Result of interface asperities distribution under compression

Using the contact mechanics model, we have studied the interfacial gap of Gore|MRC and IP|SGL under different compression pressures. We applied the model to an IP|SGL pairing and a Gore|MRC pairing. The reason for choosing this particular combination of the MPLs and CLs is its industrial (Gore|MRC) and academic (IP|SGL) application, since the IP|SGL pair is common in academic studies. Fig. 5 shows the average separation distance obtained with the model for both material sets, defined as $\delta_{av} = (\sum_{i=1}^{N}\delta_i)/N$, plotted against the average contact pressure, $p/p^* = (\sum_{i=1}^{N} p_i/p^*)/N$. For reference, based on Kundu et al.'s [41] measured Young's modulus for catalyzed Nafion membranes (~3 MPa) and an approximate Poisson ratio of 0.5, the equivalent Young's modulus to dimensionalize our non-dimensional pressure is 8 MPa. The typical average

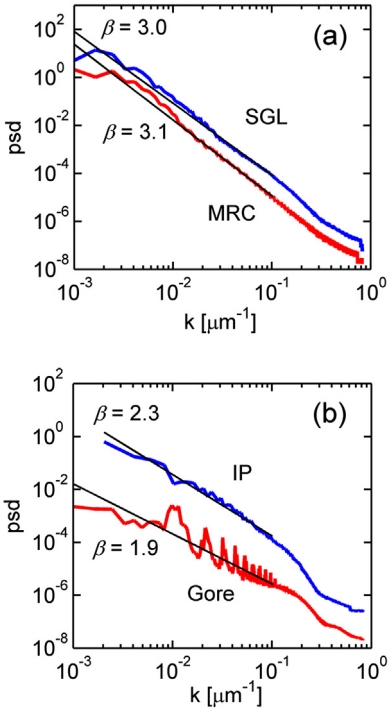

Fig. 4. Radial power spectra density curves for the MPLs (a) and CLs (b). The horizontal axis, k, is the inverse surface wave length. Straight lines represent linear fits to k values less than 10^{-1} μm^{-1}.

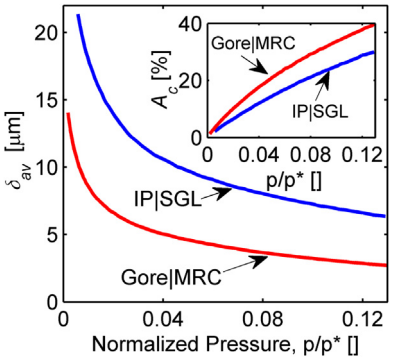

Fig. 5. Average separation distance as a function of normalized pressure. The inset shows percent area of interfacial contact.

compression pressure in PEFCs is 1 MPa, which thus corresponds to a p/p^* value of 0.125. This is comparable to the highest pressures evaluated in this study.

For both interfaces, the separation distance plotted in Fig. 5 asymptotically decreases with the increasing pressure at a similar rate. However, at all pressures, the gap between the IP|SGL is higher than the gap between the Gore|MRC due to higher degree of roughness of IP and SGL pair. It is important to note that the average separation distance is also proportional to the interfacial void volume. The relatively large δ_{av} for the IP|SGL interface is due to the wide and deep cracks in the SGL sample as visible in Fig. 3a and e. Some of the SGL cracks penetrate the whole thickness of the MPL and could be assigned to the bulk MPL morphology rather than the interfacial roughness. Here, all the cracks are treated as a part of the interface and contribute to increasing the computed interfacial gap. However, we recognize that there is a need in computational models for a distinct boundary between the inner regions of the domains and their interfaces. Our results agree reasonably well with Swamy et al. [19] who studied the interface between cracked a CL and different SGL MPLs. They estimated the average interfacial separation distance to lie in the range of 5–10 μm under homogeneous compression of 1.5 MPa. The inset of Fig. 5 shows the percentage contact area – the sum of all contact points normalized by the total area, as a function of the average contact pressure. As expected, the smoother surfaces of the Gore and MRC yield roughly 30% greater contacting area than that of the IP and SGL interface over the same range of compression pressures.

To illustrate the dependence of the interfacial void space morphology on the contact pressure, Fig. 6 images the 3D interfacial void space as a solid for the two interfaces at non-dimensional contact pressures of 0.045 and 0.12. In this case, the 0.045 case could be considered as the under-compressed morphology and the 0.12 case could be considered as the properly compressed case. For the lower 0.045 pressure case shown in Fig. 6, we observe continuous channels of void space for both interfaces. The interfacial space that forms the gap between the Gore and MRC surfaces is smoother and rounder in shape than the spiked and ridged gaps between the IP and SGL surfaces. For higher pressure shown by Fig. 6c and d, the Gore|MRC interface has large continuous contacting regions with no interfacial gap and discontinuous islands of void space. This compares well with the higher asperity contact area for the Gore|MRC in Fig. 5; as such, for the low pressure of 0.045, the contact area constitutes <20%, while for the pressure of 0.12 it is about 40%. In comparison, one observes a larger volume of the interfacial void space for the IP|SGL interface at high pressure compared to the Gore|MRC. This is attributed to the deep cracks that do not necessarily occupy proportionally large surface area but yield large interfacial void volume. The interfacial void space occupied by cracks might not have a significant impact on the contact resistance, which depends on contact surface area, but might serve for storage of liquid water during start-up and transient increases in PEFC current. This hypothesis needs further experimental evidence; the work of Owejan et al. [42] suggests that MPL cracks may not have a significant effect on the steady-state PEFC performance, whereas the work of Chun et al. [43] suggests that there is additional PEFC performance loss at high current densities due to water accumulation at the CL|MPL interface with cracked MPL.

We calculate the interface contact resistance based on electrical analogy formulated by Barber [44]:

$$R_c = \frac{1}{(\rho_{CL} + \rho_{MPL})} \frac{d\delta_{av}}{d(p/p^*)} \tag{6}$$

where the conductivities of the CL and MPL are estimated to be $\rho_{CL} = 200 S\ m^{-1}$ and $\rho_{MPL} = 300 S\ m^{-1}$ [5], respectively. Fig. 7 shows the plot of calculated contact resistance as a function of pressure for the two interfaces, where the inset is the plot on a linear scale. As expected, the value of contact resistance approaches zero at high compression pressures. Comparing the contact resistance of IP|SGL to Gore|MRC, one observes a negligible difference at high pressures due to high contact area for both pairs. At low pressures we observe a steeper decline of the resistance at the Gore|MRC interface compared to the IP|SGL interface, yielding a lower onset pressure for the asymptotic approach to zero resistance. The contact resistance results show the same trend and magnitude as Kleemann et al. [17] and Butsch et al.'s [18] experimental works, where the authors measured the contact resistance between the MPL and CL samples using a 4-point measuring device.

4.3. Void size distribution and water retention curves

Recently, there have been several studies presenting water retention curves for porous carbon substrates for fuel cell

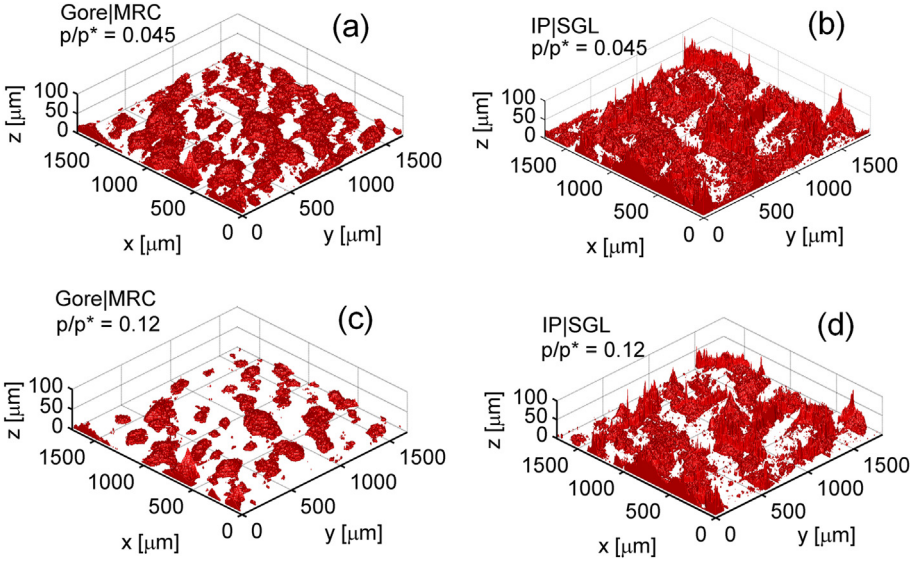

Fig. 6. Interfacial void space for Gore|MRC (a, c) and IP|SGL (b, d) interfaces at two normalized pressures of 0.045 (a, b) and 0.12 (c, d).

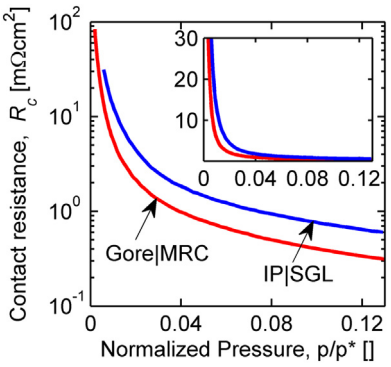

Fig. 7. Contact resistance as a function of normalized pressure.

diffusion media and electrodes, but to the best of our knowledge, there have been no studies reporting water retention curves for the CL|MPL interfaces. To bridge this gap, we extend our interface analysis to elucidate the relationships between capillary pressure and saturation for the measured interfaces. Given the local interfacial separation distance for the CL|MPL, we assume that the CL and MPL exhibit hydrophilic and hydrophobic properties, respectively [45]. Using a spherical kernel in a three-dimensional morphological opening procedure [46,47], we evaluated the percentage void space filled with a spherical hemispheres as a function of critical void radius of curvature. The shape of the kernel represents the water interface at the hydrophobic walls formed by the MPL. The procedure starts with the largest possible curvature that measurably fits into the void space, assigns that size to the corresponding voxels, and then sequentially works down in decrements of 1.8 μm until a zero radius of curvature is reached.

Fig. 8a and b plot the normalized void size distributions for the Gore|MRC and IP|SGL interfaces, respectively, at non-dimensional pressures of 0.045 and 0.12. The insets show the difference of the percent void space for a given critical radius of curvature. In other words, it highlights the change in the distribution shape with compression. We observe that the Gore|MRC interface exhibits unimodal, log-normal void size distribution, with the majority of the void volume having critical radii <15 μm. The log-normal void size distributions were previously implemented by Weber et al. [48] and Sinha et al. [49] when modeling porous PEFC diffusion media. As the inset shows, when the pressure is increased from 0.045 to 0.12, the void size distribution shifts to smaller radii, with an increased percentage of the volume in voids smaller than 10 μm and decrease relative void volume at radii between 10 and 20 μm. The percentage of void volume for radii greater than 20 μm is mostly unchanged.

The void size distribution for the IP|SGL interface (see Fig. 8b) does not have a clear log-normal distribution due to large volume with large critical radii. In addition, the distribution tail for the IP|SGL is longer than that for the Gore|MRC by roughly 10 μm. This additional large pore volume is due to the cracks observed in the SGL sample. As the inset shows, the change in the normalized void volume for the pressure increase from 0.045 to 0.12 is more broadly distributed in comparison to the Gore|MRC case.

To generate water retention curves from the aforementioned void size distributions, we need to compute capillary pressure and saturation. Capillary pressure is defined as the pressure difference between liquid and gas pressures when the interface has radius of curvature, r_c [50]. The capillary pressure can be estimated for semi-spherical water intrusion in the voids using the Young–Laplace equation:

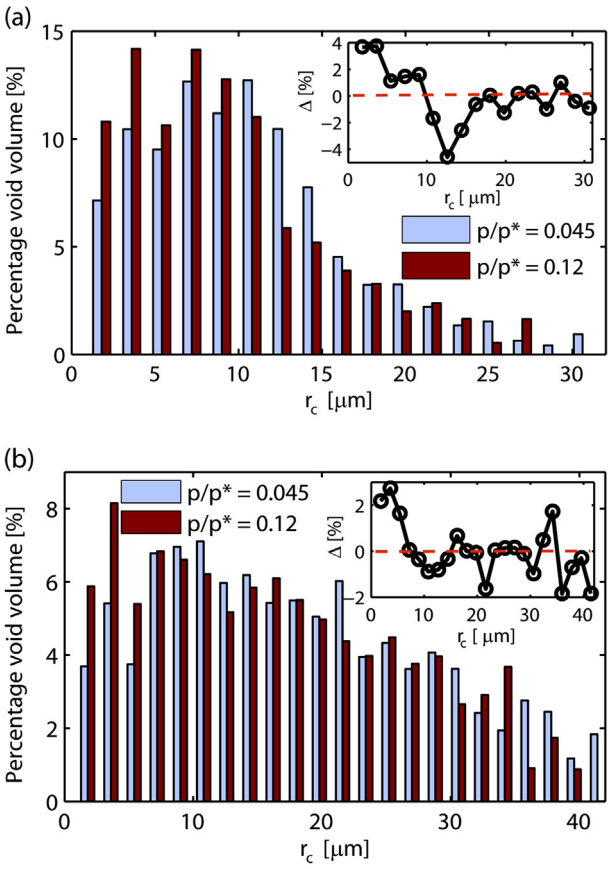

Fig. 8. Normalized void size distribution for (a) Gore|MRC and (b) IP|SGL interfaces at normalized pressures of 0.12 and 0.045. The insets show the difference in the percentage of void volume at normalized pressures 0.045 and 0.12 versus radius.

$$p_c = \frac{2\gamma}{r_c} \tag{7}$$

In using Young–Laplace equation the surfaces' wettability is not incorporated directly, however the procedure of the water intrusion into the voids incorporates the assumptions of the CL being the wetting surface and the MPL surface being ideally non-wetting. Assuming the surface tension, γ, to be a constant that can be evaluated elsewhere, we present the plot of water retention curves as a function of inverse of the critical radius of curvature instead of the capillary pressure in order to generate more general results. Starting from the largest critical radius of curvature and summing up the percentage void volume, we compute the non-wetting phase saturation for the interfacial void volume. When saturation is equal to one, the capillary pressure is high and all the hydrophobic MPL surface voids are filled with liquid water. On the other hand, for zero saturation the capillary pressure is non-existent and all the hydrophobic pores are empty. Fig. 9 plots the saturation versus the inverse critical radius of curvature for the two interfaces at the two non-dimensional pressures of 0.045 and 0.12. The figure also shows fits for van Genuchten water retention curve correlation, which can be expressed as:

$$\frac{1}{r_c} = \frac{1}{r_{cb}}\left(s^{-1/(1-1/n)} - 1\right)^{1/n} \tag{8}$$

where r_{cb} and n are fitting parameters. r_{cb} roughly represents the critical pore radius of the distribution at the 50% saturation,

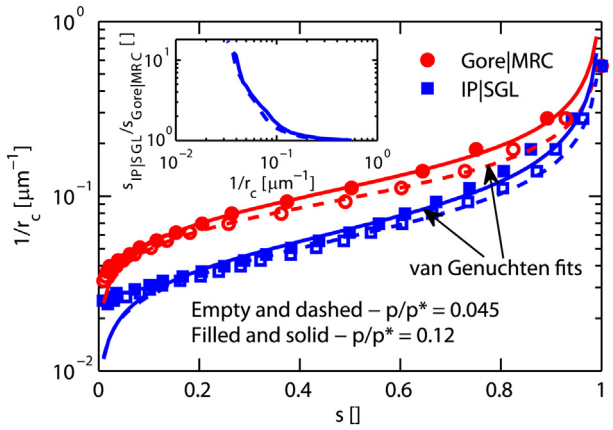

Fig. 9. The inverse radius of curvature as a function of saturation for the two MPL|CL interface sets at normalized pressures of 0.045 and 0.12. The inverse radius of curvature is proportional to the capillary pressure. The dashed and solid lines represent van Genuchten water retention curve fits. The inset shows the ratio of IP|SGL and Gore|MRC interfaces saturation for a given radius. The ratio indicates significantly higher interfacial water content in the IP|SGL interface at low liquid water pressures.

whereas n is a parameter to represent the width of the void size distribution. We assume residual saturation to be negligible.

Curve-fitting Eq. (8) for computed values of saturation and inverse radius of curvature, we extracted the van Genuchten correlation parameters shown in Table 2. We also fit the data with Brooks–Corey correlation (see Supplemental material), however the Brooks–Corey model did not capture well the overall interfacial morphology but only small region with cracks for the IP|SGL interface.

The fit of van Genuchten correlation in Fig. 9 (parameters listed in Table 2) shows a good agreement with the results of the contact mechanics model for the measured Gore and MRC surfaces for the entire range of saturation. For the IP|SGL interface, the van Genuchten correlation shows good agreement for the range of saturations between 0.15 and 1; however, at lower saturations the agreement is unsatisfactory. The regime of low non-wetting phase saturations ($s < 0.15$) corresponds to the voids accommodating large radii of curvature (low capillary pressure). This low saturation discrepancy is due to the presence of the cracks in the SGL sample, which cause the void size distribution to significantly deviate from a log-normal void size distribution for which the van Genuchten equation was developed. Comparing the Gore|MRC and IP|SGL water retention curves, we observe lower degree of saturation for the Gore|MRC for the whole range of critical radii. These trends are expected due to the fact that the IP|SGL interface has a greater amount of larger voids as shown in Fig. 8. This difference between the two pairs of samples is compounded by the fact that the average separation distance for the IP|SGL pair is roughly 100% greater than that for the Gore|MRC pair, thus entailing that at a given saturation value there is approximately twice as much accumulated water volume in the IP|SGL pairing.

We can use the results in Fig. 9 to evaluate the relative difference in interfacial water hold up between the two material sets by comparing their saturations at a given capillary pressure (i.e., critical radius of curvature). The inset of Fig. 9 presents a log–log plot of the ratio of interfacial saturations for the two material pairings as a function of inverse critical radius of curvature. The ratio has the highest value of about 11 at low capillary pressures and asymptotes to 1 at high pressures. This means the saturation of the IP|SGL interface can be up to 11 times higher than that of the Gore|MRC interface at the lowest capillary pressure (lowest saturation). Following the discussion above, the ratio of accumulated water volume is roughly twice the saturation ratio. The result shows that highly cracked CL|MPL interface can uphold up to twenty times more water compared to the smoother Gore|MRC interface.

The water retention curves in Fig. 9 have several important implications. For instance, if we consider some fixed level of water saturation in the catalyst layer with a corresponding capillary pressure, there will be a significant difference in the water accumulated in the CL|MPL interface. This could mean that during early times of transient water accumulation, the IP|SGL pair will sustain lower CL saturations as water more easily invades the low capillary pressure interface. However, during steady-state operation with a fixed value of CL saturation, there will be much more accumulated water in the IP|SGL interface. This could be up to twenty times more water. We suggest, however, that many such effects will be highly localized because of restricted in-plane water permeability given that large amounts of the interfacial void volumes exist as isolated volumes under typical PEFC compression. In other words, liquid water must propagate through the low permeability catalyst mesopores to equilibrate the pressures in adjacent voids.

Table 2
van Genuchten parameters for log-normal distributions.

	δ_{av} [μm]	r_{cb} [μm]	n [−]
Gore|MRC, $p/p^* = 0.045$	4.75	11.88	3.44
Gore|MRC, $p/p^* = 0.12$	2.78	10.63	3.127
IP|SGL, $p/p^* = 0.045$	10.01	20.83	3.018
IP|SGL, $p/p^* = 0.12$	6.41	19.48	2.805

5. Conclusions

In this paper, we applied a deterministic elastic contact mechanics model to study the CL|MPL interfacial gap under compression. The results show that the IP|SGL interface has higher degree of roughness compared to Gore|MRC interface due to highly cracked nature of the SGL sample compared to the crack-free MRC surface. This higher degree of roughness translates into two-times larger average interfacial gaps for a given pressure. For PEFC operation, large interfacial gaps at the CL|MPL interface are not desirable because they increase Ohmic resistance and present an interfacial volume that can serve as a water pooling location, leading to mass-transport losses. Our results indicate that for contact resistance, the difference between the cracked and smooth interfaces are negligible at typical compression pressures of PEFCs because cracks have large depth to width aspect ratios and thus do not occupy large surface area.

A novel aspect of the study is the reported void size distribution and water retention curves at the CL|MPL interface under different levels of compression. The more conformal Gore|MRC interface has log-normal void size distributions with increasing pore volume having critical radii <15 μm. On the other hand, the large voids due to cracks at the IP|SGL interface occupy significant percentage of interfacial void volume. These large voids can act as water-pooling volumes translating into high values of saturation and water carrying capacity. From the water retention curves, we observe that at all capillary pressures the IP|SGL interface has higher levels of saturation compared to Gore|MRC interface. This could potentially enhance fuel cell performance during start-up and increasing current transients during which water can accumulate in the cracks and large volumes, causing lower liquid saturation and better oxygen transport in the CL. Under steady-state operation conditions, our results indicate that the cracked IP|SGL sample could contain up to twenty times more water than the Gore|MRC interface at the same level of CL saturation. To further elucidate the PEFC's performance losses associated with the CL|MPL interface, the

interfacial volume and van Genuchten water retention curve correlation parameters reported here can be directly used in multiphase fuel cell models (through introduction of finite thickness interfacial domain) to estimate water accumulation and the corresponding interfacial oxygen transport resistance.

Acknowledgments

This study is supported by the National Science Foundation under Grant No. 1066623. The authors gratefully acknowledge Jon Owejan of General Motors, Inc. for supplying the MRC and Gore samples.

Appendix A. Supplementary data

Supplementary data related to this article can be found at http://dx.doi.org/10.1016/j.jpowsour.2013.03.165.

References

[1] M.K. Debe, Nature 486 (2012) 43–51.
[2] J.P. Owejan, T.A. Trabold, D.L. Jacobson, M. Arif, S.G. Kandlikar, Int. J. Hydrogen Energy 32 (2007) 4489–4502.
[3] K. Kadowaki, Y. Tabe, T. Chikahisa, ECS Trans. (2011) 431–438.
[4] S. Kim, B.K. Ahn, M.M. Mench, J. Power Sources 179 (2008) 140–146.
[5] S. Kim, M. Khandelwal, C. Chacko, M.M. Mench, J. Electrochem. Soc. 156 (2009) B99–B108.
[6] Y. Aoyama, K. Kadowaki, Y. Tabe, T. Chikahisa, ECS Trans. (2012).
[7] J.T. Gostick, M.W. Fowler, M.A. Ioannidis, M.D. Pritzker, Y.M. Volfkovich, A. Sakars, J. Power Sources 156 (2006) 375–387.
[8] S. Litster, N. Djilali, Two-phase Transport in Porous Gas Diffusion Electrodes, in: M. Faghri, B. Sunden (Eds.), Transport Phenomena in Fuel Cells, WIT Press, Southhampton, UK, 2005.
[9] J. Bear, Dynamics of Fluids in Porous Media, Dover Publications, New York, 1972.
[10] M.T. van Genuchten, Soil Sci. Soc. Am. J. 44 (1980) 892–898.
[11] K.S. Udell, Int. J. Heat Mass Transfer 28 (1985) 485–495.
[12] V.P. Schulz, J. Becker, A. Wiegmann, P.P. Mukherjee, C.Y. Wang, J. Electrochem. Soc. 154 (2007) B419–B426.
[13] E.C. Kumbur, K.V. Sharp, M.M. Mench, J. Electrochem. Soc. 154 (2007) B1295–B1304.
[14] U. Pasaogullari, C.Y. Wang, Electrochim. Acta 49 (2004) 4359–4369.
[15] K. Kang, H. Ju, J. Power Sources 194 (2009) 763–773.
[16] J.H. Nam, M. Kaviany, Int. J. Heat Mass Transfer 46 (2003) 4595–4611.
[17] J. Kleemann, F. Finsterwalder, W. Tillmetz, J. Power Sources 190 (2009) 92–102.
[18] H. Butsch, C. Roth, D. Ritzinger, G. Hoogers, A. Bock, J. Electrochem. Soc. 159 (2012) B709–B713.
[19] T. Swamy, E.C. Kumbur, M.M. Mench, J. Electrochem. Soc. 157 (2010) B77–B85.
[20] K.L. Johnson, J.A. Greenwood, J.G. Higginson, Int. J. Mech. Sci. 27 (1985) 383.
[21] J.A. Greenwood, J. ASME, Lubrication Technol 89 (1967) 81–91.
[22] R.A. Onions, J.F. Archard, J. Phys. D. Appl. Phys. 6 (1973) 289–304.
[23] A.W. Bush, R.D. Gibson, T.R. Thomas, Wear 35 (1975) 87–111.
[24] M.N. Webster, R.S. Sayles, J. Tribol.-T. ASME 108 (1986) 314–320.
[25] Y.Q. Ju, L.Q. Zheng, Wear 157 (1992) 151–161.
[26] T. Nogi, T. Kato, J. Jpn. Soc. Tribologis 42 (1997) 225–232.
[27] T. Nogi, T. Kato, J. Jpn. Soc. Tribologis 42 (1997) 158–165.
[28] Y.Z. Hu, G.C. Barber, D. Zhu, Tribol. T. 42 (1999) 443–452.
[29] Z.J. Wang, W.Z. Wang, Y.Z. Hu, H. Wang, Tribol. T. 53 (2010) 224–238.
[30] J.A. Greenwood, J.B.P. Williams, Proc. R. Soc. Lond. A. Mat. 295 (1966) 300.
[31] A.E. Love, Philos. Trans. R. Soc. London A 228 (1929) 377–420.
[32] E.O. Brigham, The Fast Fourier Transform, Prentice-Hall, 1974.
[33] S.B. Liu, Q. Wang, G. Liu, Wear 243 (2000) 101–111.
[34] R.W. Cottle, J.S. Pang, R.E. Stone, The Linear Complementarity Problem, Academic Press, 2009.
[35] F.E. Hizir, S.O. Ural, E.C. Kumbur, M.M. Mench, J. Power Sources 195 (2010) 3463–3471.
[36] Method for the Assesment of Surface Texture (1972).
[37] J.M. Bennett, L. Mattsson, Introduction to Surface Roughness and Scattering, Optical Society of America, Washington, D.C, 1989.
[38] E. Trujillo, J.A. Ramirez, K.J. Elder, Hydrol. Process. 23 (2009) 1575–1590.
[39] E. Trujillo, J.A. Ramirez, K.J. Elder, Water Resour. Res. 43 (2007).
[40] C. De Michele, P. Bernardara, Atmos. Res. 77 (2005) 124–136.
[41] S. Kundu, L.C. Simon, M. Fowler, S. Grot, Polymer 46 (2005) 11707–11715.
[42] J.P. Owejan, J.E. Owejan, W.B. Gu, T.A. Trabold, T.W. Tighe, M.F. Mathias, J. Electrochem. Soc. 157 (2010) B1456–B1464.
[43] J.H. Chun, D.H. Jo, S.G. Kim, S.H. Park, C.H. Lee, S.H. Kim, Renew. Energy 48 (2012) 35–41.
[44] J.R. Barber, Proc. R. Soc. London A. Mat. 459 (2003) 53–66.
[45] S. Litster, G. McLean, J. Power Sources 130 (2004) 61–76.
[46] J. Serra, Image Analysis and Mathematical Morphology, Academic Press, London, UK, 1982.
[47] J. Serra, Image Analysis and Mathematical Morphology: Theoretical Advances, Theoretical Advances, London, UK, 1988.
[48] A.Z. Weber, R.M. Darling, J. Newman, J. Electrochem. Soc. 151 (2004) A1715–A1727.
[49] P.K. Sinha, P.P. Mukherjee, C.Y. Wang, J. Mater. Chem. 17 (2007) 3089–3103.
[50] F.A. Dullien, Porous Media: Fluid Transport and Pore Structure, second ed., Academic Press, Inc., New York, 1992.

Nomenclature

A: surface area (μm^2)
A_c: percent contact area (%)
C: the matrix of influence coefficients (μm)
E_{eq}: equivalent Young's modulus defined by Eq. (3)
K: kernel defined by Eq. (2)
N: total number of discrete elements
P: normalized pore volume
R: roughness (μm)
R_c: contact resistance, ($m\Omega\ cm^2$)
k: vector frequency, ($\mu\ m^{-1}$)
n: van Genuchten fitting parameter
p/p^*: normalized compression pressure
psd: power spectrum density
$\bar{r}$: mean pore radius (μm)
r_c: critical radius of curvature (μm)
r_{cb}: critical void radius of curvature of the van Genuchten distribution (μm)
s: saturation
u: composite surface displacement (μm)

Greek letters
Δ: percentage difference between the high and low pressure void volumes, (%)
β: exponent of psd linear fits
δ: interfacial gap (μm)
$\bar{\delta}$: undeformed interfacial gap (μm)
γ: surface tension ($N\ m^{-1}$)
σ_{psd}: log-normal standard deviation
θ: contact angle
ρ: conductivity ($S\ m^{-1}$)
ν: Poisson's ratio

Subscripts
CL: catalyst layer
MPL: micro-porous layer